JOURNAL OF GUIDANCE, CONTROL, AND DYNAMICS
Vol. 25, No. 6, November–December 2002

# Adaptive Estimation Methodology for Helicopter Blade Structural Damage Detection

Jonathan Alkahe,* Yaakov Oshman,† and Omri Rand‡
*Technion—Israel Institute of Technology, Haifa 32000, Israel*

**A new, multiple model approach for detection and identification of structural damage in a rotating helicopter blade is presented. A full-scale rotor analysis using a detailed model of the hingeless blade elastic behavior and dynamics is carried out. Several stiffness damage levels and locations are considered, and a set of Kalman filters is constructed accordingly. The best fitting model is determined in a probabilistic manner. Because the new method is model-based, the need for a training stage is eliminated, and a wide range of flight regimes can be handled. Moreover, process and measurement noises are treated inherently, contributing to the superiority of the method over previously published related methods. A Monte Carlo simulation study is used to provide a comprehensive analysis of the statistical nature of the method. Single-blade analysis results demonstrate excellent identification capability and good damage detection in the presence of a relatively high level of noise. The case of damage located near the blade's root combined with a sensor near the tip produces a high damage identification probability. In less detectable cases, such as damage located in midspan, a simple statistical procedure enables achieving a high detection probability along with a low false alarm rate.**

## Nomenclature

$\boldsymbol{A}_j$ = $j$th filter residual covariance matrix
$\boldsymbol{a}$ = vector of unknown parameters (fault influence)
$\boldsymbol{B}$ = continuous-time control matrix
$\boldsymbol{F}$ = continuous-time state transition matrix
$\boldsymbol{G}$ = continuous-time process noise distribution model
$\boldsymbol{H}$ = measurement matrix
$N$ = number of single-run repetitions
$n$ = number of runs where damage was detected
$n_d$ = predetermined threshold
$\boldsymbol{P}$ = filter error covariance matrix
$P_D$ = overall detection probability
$P_{\mathrm{FA}}$ = overall false alarm probability
$p$ = probability
$p_D$ = single-run detection probability
$p_{\mathrm{FA}}$ = single-run false alarm probability
$\boldsymbol{Q}_d$ = discrete-time process noise covariance matrix
$q$ = fitness probability
$\boldsymbol{R}$ = measurement noise variance matrix
$\boldsymbol{r}$ = residual vector
$\boldsymbol{u}$ = control vector
$\boldsymbol{v}$ = measurement noise vector
$\boldsymbol{w}$ = process noise vector
$\boldsymbol{w}_d$ = equivalent discrete-time process noise vector
$\boldsymbol{x}$ = state vector
$x_d$ = damage location along the blade's span (measured from root)
$x_s$ = sensor location along the blade's span (measured from root)
$\hat{\boldsymbol{x}}_j$ = $j$th filter predicted state estimate
$\boldsymbol{Z}_i$ = measurement history from the first sample until sample time $t_i$
$\boldsymbol{z}$ = measurement vector
$\boldsymbol{\Theta}$ = mode shape matrix
$\boldsymbol{\xi}$ = vector of elastic mode participating factors
$\boldsymbol{\Phi}$ = state transition matrix
$\boldsymbol{\Psi}$ = control matrix

Presented as Paper 2000-4569 at the AIAA Guidance, Navigation, and Control Conference, Denver, CO, 14–17 August 2000; received 13 August 2001; revision received 22 July 2002; accepted for publication 24 July 2002. 

*Graduate Student, Department of Aerospace Engineering.
†Associate Professor, Department of Aerospace Engineering; yaakov.oshman@technion.ac.il. Associate Fellow AIAA.
‡Associate Professor, Department of Aerospace Engineering; aeromri@aerodyne.technion.ac.il.

## I. Introduction

THE detection of damage as a part of self-health monitoring in structural systems is an important contributor to their safety, reliability, and structural integrity. Early damage detection has the potential of reducing life-cycle costs and possibly increasing replacement time intervals. If damage is located and monitored, then components of the structure may be replaced before some critical point is reached and a dangerous failure occurs.

Cracks found in structural elements have various causes. One form of crack is caused by fatigue and takes place under service conditions as a result of the limited fatigue strength. Cracks may also appear due to mechanical defects or manufacturing processes. Cracks present a serious threat to proper performance, and most failures of presently used equipment are due to material fatigue. For this reason, methods enabling early detection and localization of cracks have been the subject of many studies.[1–6]

One approach for damage detection in beam structures described in the literature is based on using a subspace rotation algorithm.[1] This method views damage location and damage extent as two different problems requiring two separate solutions. In this approach, damage is manifested as changes in the mass, damping, and stiffness matrices of the structure. Strain sensors were used; therefore, a method for extracting displacement frequency responses from strain data was presented. This study shows that higher-order vibration modes are required to locate damage events. In addition, condensation methods cannot be used to remove rotational degrees of freedom because of their coupling with translation degrees of freedom.

Another class of damage detection methods in which damage is seen as a change in the parameters of a structural model is based on modal information. Typically, modal-based damage detection methods use a finite element model of the system combined with experimental modal data to determine damage location and extent. The effect of cracks on the natural frequencies of a cantilevered beam is demonstrated in Ref. 2. In their study, the authors assumed that the cracks occur in the first mode of fracture, that is, the crack

opening mode. These cracks were modeled using rotational springs with equivalent stiffnesses. The natural frequencies were calculated by solving the beam's deflection partial differential equation with the appropriate boundary conditions at the crack locations. The positions of two cracks in relation to each other, in addition to the changes in crack depths, were shown to affect the beam's natural frequencies. However, only the first mode was shown, and no information was given regarding the effect of the cracks relative to an undamaged beam. The work presented in Ref. 3 also applies a rotational spring to model the crack when the crack is open. The crack parameters (size and location) are to be extracted by examining two crack signatures calculated by subjecting the beam to harmonic loading at two frequencies that would excite the first and second modes. These crack signatures are calculated using Fourier transforms of the displacement at a specific point along the beam and are shown to be very small. Because natural frequencies change very slightly as crack size and location varies, the addition of noise, not treated in this work, would significantly decrease the identification capability. In Ref. 4, the changes in mode shape due to presence of structural damage were determined. A finite element model with reductions of the modulus of elasticity in prescribed segments was implemented. It was shown that the elastic rotation undergoes a step jump in value when crossing the damage location, whereas the displacement parameter takes a change in its slope. An eigenstructure assignment technique for damage detection in rotating structures is demonstrated in Ref. 5. The damage is simulated by a 10% loss of mass and stiffness in the damaged element. The eigenvector that best approximates the damaged eigenvector is obtained, and the angle between these two vectors is evaluated. This process is repeated for every one of the modes considered. A test case with noise-contaminated mode shapes is also presented. An extension to this algorithm for rotating helicopter blades accounting for hovering aerodynamics is presented in Ref. 7. The blade's aerodynamics is incorporated as a damping term in the structural dynamics of the blade. The damage is shown to be properly characterized when flapping modes are used. However, the algorithm presented is based on a least-squares estimation procedure, which can prove to perform poorly in some cases.

In the present study, the damage detection methodology is based on the multiple-model approach. In this method, various damage locations and levels are considered, where each case is adequately represented by a finite element model. A Kalman filter is tuned according to each model, and the best fitting one is determined in a probabilistic manner based on noisy displacement or velocity measurements. This approach eliminates the need for a training stage that characterizes other methods, like the fault detection and identification (FDI) algorithms based on neural networks. Additional important features of the proposed approach are the inherent treatment of process noise, which enables the inclusion of modeling uncertainties, as well as the filtering of measurement noise, which is done in a manner much more efficient than averaging techniques commonly used. That each one of the filters is based on a model of the dynamic system contributes to the flexibility of the algorithm by allowing a direct access to perform frequent changes and updates in the models. Another key advantage, using the proposed FDI algorithm, is the judgment and decision-making process, which is optionally left to the human operator due to the probabilistic nature of the results.

The remainder of this paper is organized as follows: In the next section, a detailed discussion of the multiple-model adaptive estimation (MMAE) approach, adopted as an FDI methodology, is presented. This is followed by a formulation of the blade model used in the present analysis. A damage identification decision logic is also presented to complete the FDI algorithm. Several numerical studies are shown, including a case of a single blade and a full-scale, fixed-shaft rotor, followed by concluding remarks.

## II. MMAE

In various estimation problems, specifically in damage detection cases, uncertain parameters exist within the system model used for algorithm design. Typically, these parameters can undergo large jump changes. Such problems give rise to the need for estimation of parameter values simultaneously with estimation of state variables. One means of accomplishing this is the MMAE technique.[8,9] The system is assumed to be adequately representable by a linear stochastic state model, with uncertain parameters affecting the matrices defining the structure of the model or the noise distribution model. It is further assumed that the parameters can take only discrete values. In cases where continuous parameter values are presented, representative discrete values have to be chosen throughout the continuous range of possible values. A Kalman filter[10] is then designed for each choice of parameter value, resulting in a bank of $K$ separate filters, designated $\boldsymbol{r}_j$ for the $j$th filter [see Fig. 1 and Eq. (14)] the conditional probabilities of each discrete parameter value being "correct" (given the measurement history to that time) are evaluated recursively. Note that the estimated $j$th filter state vector $\hat{\boldsymbol{x}}_j$ is not used in this damage detection application.

Following the development presented in Refs. 9 and 11, consider the system model described by the first-order, linear, stochastic differential state equation of the form

$$\dot{\boldsymbol{x}}(t) = \boldsymbol{F}(\boldsymbol{a}, t)\boldsymbol{x}(t) + \boldsymbol{G}(\boldsymbol{a}, t)\boldsymbol{w}(t) + \boldsymbol{B}(\boldsymbol{a}, t)\boldsymbol{u}(t) \tag{1}$$

with noisy measurements described by the discrete time equation

$$\boldsymbol{z}_k = \boldsymbol{H}_k(\boldsymbol{a})\boldsymbol{x}_k + \boldsymbol{v}_k \tag{2}$$

where $\boldsymbol{x}(t)$ is the system state vector and $\boldsymbol{u}(t)$ is the control vector. Here, $\boldsymbol{x}_k$ and $\boldsymbol{z}_k$ are the state and measurement vectors at the discrete time $t_k$, respectively. It is assumed that the process noise vector $\boldsymbol{w}(t)$ and the discrete measurement noise vector $\boldsymbol{v}_k$ are independent, zero-mean, white Gaussian noise processes with covariances

$$\mathbb{E}\{\boldsymbol{w}(t)\boldsymbol{w}^T(s)\} = \boldsymbol{Q}(t)\delta(t-s) \tag{3}$$

$$\mathbb{E}\{\boldsymbol{v}(t_i)\boldsymbol{v}^T(t_j)\} = \boldsymbol{R}(t_i)\delta_{ij} \tag{4}$$

where $\delta_{ij}$ is Kronecker's delta function, $\boldsymbol{a}$ is a vector containing the structural damage effects, $\boldsymbol{F}(\boldsymbol{a}, t)$ is the state transition matrix, $\boldsymbol{G}(\boldsymbol{a}, t)$ is the process noise distribution model, $\boldsymbol{B}(\boldsymbol{a}, t)$ is the control matrix, and $\boldsymbol{H}_k(\boldsymbol{a})$ is the measurement matrix at time $t_k$. In the case of a discrete stochastic state propagation model, Eq. (1) is replaced by the following equation:

$$\boldsymbol{x}_{k+1} = \boldsymbol{\Phi}_{k+1,k}(\boldsymbol{a})\boldsymbol{x}_k + \boldsymbol{w}_{dk} + \boldsymbol{\Psi}_{k+1,k}(\boldsymbol{a})\boldsymbol{u}_k \tag{5}$$

Assuming that the dynamic system is quasi-stationary, the following relations hold:

$$\boldsymbol{\Phi}_{k+1,k}(\boldsymbol{a}) = e^{\boldsymbol{F}_k(a)\Delta t} \tag{6}$$

$$\boldsymbol{\Psi}_{k+1,k}(\boldsymbol{a}) = \boldsymbol{B}_k(\boldsymbol{a})\Delta t \tag{7}$$

where

$$\boldsymbol{F}_k(\boldsymbol{a}) = \boldsymbol{F}(\boldsymbol{a}, t)\,|_{t=t_k} \tag{8a}$$

$$\boldsymbol{B}_k(\boldsymbol{a}) = \boldsymbol{B}(\boldsymbol{a}, t)\,|_{t=t_k} \tag{8b}$$

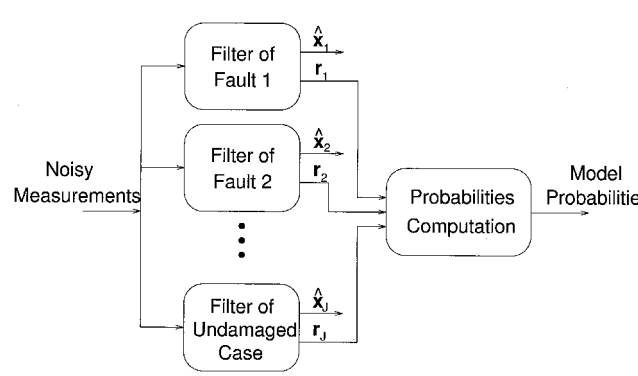


**Fig. 1 MMAE procedure ($\hat{x}_j$ and $r_j$ are the $j$th filter state estimate and residual vectors, respectively).**

and $\Delta t$ is the discretization time interval. Then, $\boldsymbol{w}_{d_k}$ is the equivalent discrete-time process noise vector with the covariance

$$\mathbb{E}\left\{\boldsymbol{w}_{d_i}\boldsymbol{w}_{d_j}^T\right\} = \boldsymbol{Q}_{d_i}\delta_{ij} \tag{9}$$

where $\boldsymbol{Q}_{d_i}$ is calculated using the relation

$$\boldsymbol{Q}_{d_i} = \boldsymbol{G}_i\boldsymbol{Q}(t_i)\boldsymbol{G}_i^T\,\Delta t \tag{10}$$

where

$$\boldsymbol{G}_k(\boldsymbol{a}) = \boldsymbol{G}(\boldsymbol{a}, t)\mid_{t=t_k} \tag{11}$$

Because $\boldsymbol{a}$ may assume a continuous range of values over the space of allowable parameters, it is necessary to discretize $\boldsymbol{a}$ into a set of $J$ vector values: $\boldsymbol{a}_1, \boldsymbol{a}_2, \ldots, \boldsymbol{a}_J$. An MMAE consists of $J$ independent Kalman filters, in which the $j$th filter is constructed according to a specific parameter value $\boldsymbol{a}_j$. These $J$ filters form a bank of elemental filters that are processed in parallel. Each elemental filter produces its own estimate of the true state, denoted as $\hat{\boldsymbol{x}}_j(t_i)$, for the $j$th hypothesized value of $\boldsymbol{a}$. The residuals of all $J$ elemental filters are then used to calculate the probability that $\boldsymbol{a}$ assumes the value $\boldsymbol{a}_j$ at time $t_i$, for $j = 1, 2, \ldots, J$. This probability is called the "hypothesis conditional probability" and is denoted as $p_j(t_i)$. This conditional probability represents the validity of the $j$th filter's system model at time $t_i$. The hypothesis conditional probabilities $p_j(t_i)$, $j = 1, 2, \ldots, J$, are calculated at each sample time $t_i$, by the recursive equation

$$p_j(t_i) = \frac{f_{z[t_i|a,Z(t_{i-1})]}(\boldsymbol{z}_i|\boldsymbol{a}_j, \boldsymbol{Z}_{i-1})\,p_j(t_{i-1})}{\sum_{k=1}^{J} f_{z[t_i|a,Z(t_{i-1})]}(\boldsymbol{z}_i|\boldsymbol{a}_j, \boldsymbol{Z}_{i-1})\,p_k(t_{i-1})} \tag{12}$$

where $\boldsymbol{Z}(t_{i-1})$ is the measurement history from the first sample time until sample time $t_{i-1}$, and

$$f_{z[t_i|a,Z(t_{i-1})]}(z_i|a_j, Z_{i-1}) = \left[1\Big/(2\pi)^{S/2}|\boldsymbol{A}_j(t_i)|^{\frac{1}{2}}\right]\exp\left\{-\tfrac{1}{2}\boldsymbol{r}_j^T(t_i)\boldsymbol{A}_j^{-1}(t_i)\boldsymbol{r}_j(t_i)\right\} \tag{13}$$

where $S$ is the number of sensors. The $j$th filter residual vector is

$$\boldsymbol{r}_j(t_i) = \boldsymbol{z}(t_i) - \boldsymbol{H}_j(t_i)\hat{\boldsymbol{x}}_j\left(t_i^-\right) \tag{14}$$

where $\hat{\boldsymbol{x}}_j(t_i^-)$ is the $j$th filter predicted state estimate. The $j$th filter-computed residual covariance matrix $\boldsymbol{A}_j(t_i)$ is calculated by

$$\boldsymbol{A}_j(t_i) = \boldsymbol{H}_j(t_i)\boldsymbol{P}_j\left(t_i^-\right)\boldsymbol{H}_j^T(t_i) + \boldsymbol{R}_j(t_i) \tag{15}$$

where $\boldsymbol{P}_j(t_i^-)$ is the $j$th filter prediction error covariance. The residual of the $j$th filter plays a major role in determining $p_j(t_i)$. As is evident from Eq. (12), the filter with the smallest value of $\boldsymbol{r}_j^T(t_i)\boldsymbol{A}_j^{-1}(t_i)\boldsymbol{r}_j(t_i)$ assumes the largest conditional hypothesis probability. Thus, this algorithm is consistent with the intuition that the residuals of a well-matched filter should be smaller (relative to the filter's internally computed residual covariance $\boldsymbol{A}_j$) than the residuals of a mismatched filter. To allow the estimator to adapt to the changing parameter value, the hypothesis conditional probabilities are artificially bounded below by a small number, taken in this study to be 0.0005. This ensures preventing any of them from converging to zero, which would make it very difficult for them to change significantly in response to a subsequent change in true parameter value. The MMAE procedure is summarized in Fig. 1.

## III. Blade Model

### A. Blade Elements

To use the multiple-model approach just presented, the structural model of a rotating blade must first be determined. The development of a finite element (FE) model of an Euler–Bernoulli beam in bending, representing the blade, follows.

A blade element is shown in Fig. 2. At each end there are two local degrees of freedom, one for vertical translation $w$ and one for rotation $\theta$, resulting in a total of four degrees of freedom per

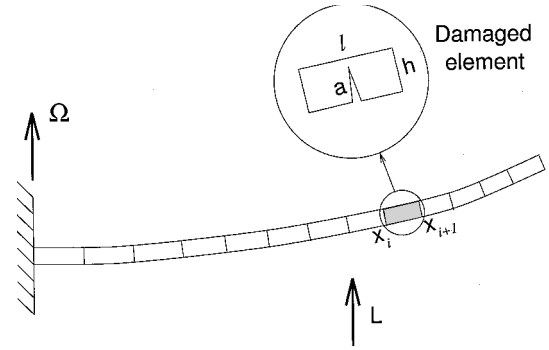


**Fig. 2 Damaged blade model.**

element. The structural model representative of a blade element with no damping must, therefore, comprise a $4 \times 4$ mass matrix and a $4 \times 4$ stiffness matrix that couple the vertical translations and rotations. For a uniform $i$th blade element, the elemental mass and stiffness matrices are as follows[12]:

$$(m_e)_i = \lambda_i\ell\begin{bmatrix} \frac{13}{35} & \frac{11}{210}\ell & \frac{9}{70} & -\frac{13}{420}\ell \\ & \frac{1}{105}\ell^2 & \frac{13}{420}\ell & -\frac{1}{140}\ell^2 \\ & \text{sym} & \frac{13}{35} & -\frac{11}{210}\ell \\ & & & \frac{1}{105}\ell^2 \end{bmatrix}_i \tag{16}$$

$$(k_e)_i = (EI_0)_i\begin{bmatrix} \frac{12}{\ell^3} & \frac{6}{\ell^2} & -\frac{12}{\ell^3} & \frac{6}{\ell^2} \\ & \frac{4}{\ell} & -\frac{6}{\ell^2} & \frac{2}{\ell} \\ & \text{sym} & \frac{12}{\ell^3} & -\frac{6}{\ell^2} \\ & & & \frac{4}{\ell} \end{bmatrix}_i$$

$$+\frac{\Omega^2 J_i}{2}\begin{bmatrix} \frac{6}{5\ell} & \frac{1}{10} & -\frac{6}{5\ell} & \frac{1}{10} \\ & \frac{2\ell}{15} & -\frac{1}{10} & -\frac{\ell}{30} \\ & \text{sym} & \frac{6}{5\ell} & -\frac{1}{10} \\ & & & \frac{2\ell}{15} \end{bmatrix}_i$$

$$-\lambda_i\ell_i\Omega^2\begin{bmatrix} \frac{3x_i}{5}+\frac{6\ell}{35} & \frac{\ell x_i}{10}+\frac{\ell^2}{28} & -\frac{3x_i}{5}-\frac{6\ell}{35} & -\frac{\ell^2}{70} \\ & \frac{\ell^2 x_i}{30}+\frac{\ell^3}{105} & -\frac{\ell x_i}{10}-\frac{\ell^2}{28} & -\frac{\ell^2 x_i}{60}+\frac{\ell^3}{70} \\ & \text{sym} & \frac{3x_i}{5}+\frac{6\ell}{35} & \frac{\ell^2}{70} \\ & & & \frac{\ell^2 x_i}{10}+\frac{\ell^3}{70} \end{bmatrix}_i \tag{17}$$

where

$$J_i = \sum_{j=i}^{N}\lambda_j\ell_j\left(x_{j+1}^2 - x_j^2\right) \tag{18}$$

and $\lambda_i$ is the $i$th element mass per unit length, $(EI_0)_i$ is the $i$th element undamaged stiffness, $x_i$ is the $i$th element position (first

node location, see Fig. 2), and $\ell_i$ is the $i$th element length. These elemental matrices can be assembled into global matrices representing the entire blade, where coefficients of the elemental matrices of one blade element are added to the coefficients of the elemental matrices of another blade element that shares a common node. The global mass, damping, and stiffness matrices, denoted $\boldsymbol{M}(\boldsymbol{a})$, $\boldsymbol{C}(\boldsymbol{a})$, and $\boldsymbol{K}(\boldsymbol{a})$, respectively, are used to construct the continuous state transition matrix, $\boldsymbol{F}(\boldsymbol{a})$ [see Eq. (1)] as follows:

$$\boldsymbol{F}(\boldsymbol{a}) = \begin{bmatrix} \mathbf{0} & \boldsymbol{I} \\ -\boldsymbol{M}(\boldsymbol{a})^{-1}\boldsymbol{K}(\boldsymbol{a}) & -\boldsymbol{M}(\boldsymbol{a})^{-1}\boldsymbol{C}(\boldsymbol{a}) \end{bmatrix} \tag{19}$$

### B. Calculation of the Reduced Stiffness

Consider a cracked section of the blade, illustrated in Fig. 2. The calculation of the reduced stiffness of the cracked portion of the blade is based on concepts of linear elastic fracture mechanics and Castigliano's theorem (see Ref. 2). The potential energy of the cracked section of the blade can be regarded as the sum of a potential energy that would exist in an undamaged state and an additional term due to the presence of the crack:

$$V = V_0 + V_c \tag{20}$$

The angle of rotation is expressed using Castigliano's theorem as follows:

$$\theta \triangleq \frac{\partial V_0}{\partial M} + \frac{\partial V_c}{\partial M} = \theta_0 + \theta_c \tag{21}$$

The potential energy associated with the crack is evaluated by integrating the energy release rate over the crack area

$$V_c = \int_A \frac{1}{2}\sigma\varepsilon \, \mathrm{d}A = \int_0^{ab} \frac{K_I^2}{E} \, \mathrm{d}A \tag{22}$$

where $K_I$ is the stress intensity factor for mode $I$ and $b$ is the blade width. Combination of Eqs. (21) and (22) gives an expression of $\theta_c$ in terms of $K_I$,

$$\theta_c = \int_0^{ab} \frac{2}{E} K_I \frac{\partial K_I}{\partial M} \, \mathrm{d}A \tag{23}$$

The stress intensity factor, which depends on the type of loading, can be expressed as follows:

$$K_I = (6M/bh^2)\sqrt{\pi a}F(a/h) \tag{24}$$

where

$$F(a/h) = 1.122 - 1.4(a/h) + 7.33(a/h)^2 - 13.08(a/h)^3 + 14(a/h)^4 \tag{25}$$

where $a$ is the crack length and $h$ is the blade thickness (see Fig. 2). Substituting Eqs. (25) and (24) in Eq. (23) and integrating yields

$$\theta_c = (72\pi M/Ebh^2)F_1(a/h) \tag{26}$$

where

$$F_1(a/h) = 19.6(a/h)^{10} - 40.693(a/h)^9 + 47.04(a/h)^8 - 32.993(a/h)^7 + 20.294(a/h)^6 - 9.975(a/h)^5 + 4.602(a/h)^4 - 1.047(a/h)^3 + 0.629(a/h)^2 \tag{27}$$

From Eq. (27), it is evident that this formulation is valid only for small cracks because $F_1(a/h)$ has a finite value for $a/h = 1$. It is also assumed that the blade's response is symmetric for a symmetric excitation. The angle of rotation of the cracked section of the blade is, therefore, given by

$$\theta \triangleq M\ell/EI_c = M\ell/EI_0 + (72\pi M/Ebh^2)F_1(a/h) \tag{28}$$

which yields

$$\frac{EI_c}{EI_0} = \frac{1}{1 + 6\pi(h/\ell)F_1(a/h)} \tag{29}$$

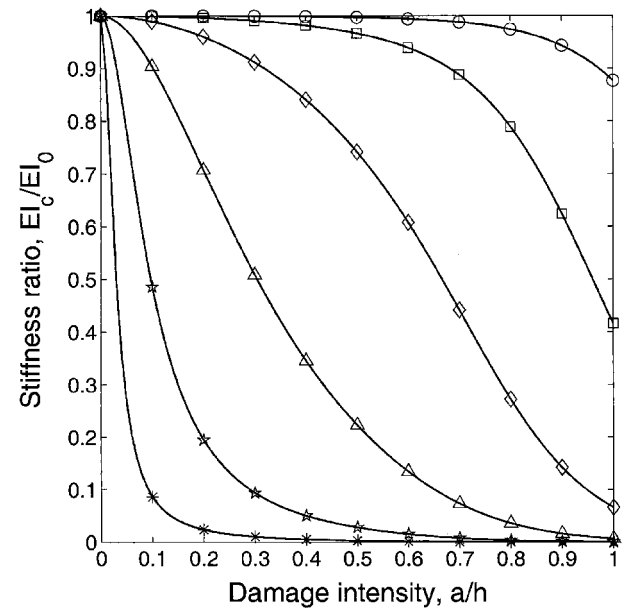


**Fig. 3 Cracked element stiffness to baseline stiffness ratio vs crack intensity: ○, $h/\ell = 0.001$; □, $h/\ell = 0.01$; ◇, $h/\ell = 0.1$; △, $h/\ell = 1$; ☆, $h/\ell = 10$; and ∗, $h/\ell = 100$.**

where $\ell$ is the section length. The cracked element stiffness to baseline stiffness $EI_c/EI_0$, as a function of the crack intensity $a/h$ and the blade thickness to element length ratio $h/\ell$, is shown in Fig. 3. Evidently, to describe correctly that damage caused by a crack is a local phenomenon, the ratio $h/\ell$ must be sufficiently large; therefore, refinement of the element meshing is essential near the crack.

*Remark 1*: Although the present study assumes that the damaged blade's response is symmetric for symmetric excitation, nonsymmetric response can be handled by the proposed FDI method as well. Note, however, that modeling the blade's response in the nonsymmetric case would be significantly more complex than in the symmetric case discussed herein.

## IV. Damage Identification Decision Logic

The damage detection algorithm consists of five different models running in parallel: four damaged blade models along with the baseline undamaged blade model. These models are designated as 0 for the baseline model and 1–4 for the damaged blade models. The modeled damage, reflected by reduced stiffness values, is assumed to be located at one of four equally spaced spanwise locations, that is, elements 3, 7, 11, or 15. The true damage may occur at 10 equally spaced elements along the blade, that is, elements 2, 4, 6, . . . , 20. Note that the true damage location is not congruent with the filter locations. Therefore, one of this study's objectives is to verify that the filter with the closest damage location (the most suitable to describe the true damaged blade behavior) indeed receives the highest probability.

The damage detection process, which is based on a detection time interval, designated as $t_p$, is termed, in this study, a single-run detection process. The decision logic is based on calculating the fitness probability for each of the models over a decision time interval (designated as $t_d$). Let $p_j(t_i)$ denote the hypothesis conditional probability of the $j$th model at a discrete time $t_i$ [see Eq. (12)], and let $q_j$ refer to the fitness probability of the $j$th model. Then,

$$q_j = \frac{\sum_{t \in t_d} p_j(t)}{\sum_{k=1}^{J} \sum_{t \in t_d} p_k(t)} \tag{30}$$

Let $q_{\max}$ be defined as

$$q_{\max} \triangleq \max_{j \in \{1,2,\ldots,J\}} \{q_j\} \tag{31}$$

The model associated with $q_{\max}$ is said to describe the true damaged behavior in the best manner. Because there are 11 possible locations of the true damage (zero means no damage), and 10 different

sensor locations, the total number of cases inspected equals 110. Although measurement noise is filtered, the possibility of getting different identification results while examining the same damaged case still exists due to the stochastic nature of the noise. To provide a better view of the statistical nature of the results, a Monte Carlo analysis is carried out, where the same damaged case is repeated, albeit with different noise values. For each one of the possible 110 cases, the Monte Carlo procedure continues until the identification probability of the model, found to be the most fitting, converges. In any case, an upper limit of 150 Monte Carlo runs is set. This procedure results in estimated probability values for the single-run process. When the true case is the case of no damage, the single-run false alarm rate, designated by $p_{\mathrm{FA}}$, is calculated. Single-run detection and identification probabilities result for each one of the cases where a fault occurs. These probabilities are designated by $p_D$ and $p_I$, respectively.

## V. Statistical Experiment

The overall false alarm and detection probabilities can be controlled using a well-designed statistical experiment. Let $H_0$ and $H_1$ denote the hypotheses of "no damage" and "damage," respectively. Assume that $N$ is the total number of single-run repetitions and $n$ is the number of runs in which damage was detected. A decision criterion is defined as follows:

$$n \underset{H_0}{\overset{H_1}{\gtrless}} n_d \tag{32}$$

where $n_d$ is a predetermined threshold. When the true undamaged case is not detected, a false alarm results (type 1 error). The false alarm probability is calculated using the following expression:

$$P_{\mathrm{FA}} \triangleq P(H_1|H_0) = \sum_{i=n_d}^{N} \binom{N}{i} p_{\mathrm{FA}}^{i} (1 - p_{\mathrm{FA}})^{N-i} \tag{33}$$

When true damage is not detected, a missed detection (or type 2 error) occurs. This probability is calculated as follows:

$$P_{\mathrm{MD}} = 1 - P_D \triangleq P(H_0|H_1) = \sum_{i=1}^{n_d - 1} \binom{N}{i} (1 - p_D)^{i} p_D^{N-i} \tag{34}$$

A detector operating characteristics plot, showing $P_D$ vs $P_{\mathrm{FA}}$, can be constructed. With this plot, the total number of runs and the threshold level can be tuned to achieve an overall low false alarm rate combined with a high detection probability.

## VI. Simulation Study

The detection and identification capabilities of the proposed method are demonstrated through two test cases of a deformed rotating blade: an elastic flapping blade in vacuum and a full-scale rotor with flap, lead-lag, and twist elastic motions.

### A. Elastic Flapping Blade

Consider a rotating cantilevered blade in vacuum, with properties as listed in Table 1. A schematic representation of the damaged blade is shown in Fig. 2. The blade is divided into 20 equally spaced elements. The baseline damaged case consists of a crack with a ratio $a/h$ of 0.2. A modal analysis is then carried out by applying the transformation

$$\boldsymbol{x}_k = \boldsymbol{\Theta}(\boldsymbol{a})\boldsymbol{\xi}_k \tag{35}$$

where $\boldsymbol{\Theta}(\boldsymbol{a})$ is the modal shape matrix for a given damaged case. The blade's equation of motion, represented by

$$\boldsymbol{M}(\boldsymbol{a})\ddot{\boldsymbol{x}} + \boldsymbol{C}(\boldsymbol{a})\dot{\boldsymbol{x}} + \boldsymbol{K}(\boldsymbol{a})\boldsymbol{x} = \boldsymbol{u}(t) \tag{36}$$

now becomes

$$\bar{\boldsymbol{M}}(\boldsymbol{a})\ddot{\boldsymbol{\xi}} + \bar{\boldsymbol{C}}(\boldsymbol{a})\dot{\boldsymbol{\xi}} + \bar{\boldsymbol{K}}(\boldsymbol{a})\boldsymbol{\xi} = \bar{\boldsymbol{u}}(t) \tag{37}$$

where

$$\bar{\boldsymbol{M}}(\boldsymbol{a}) \triangleq \boldsymbol{\Theta}(\boldsymbol{a})^T \boldsymbol{M}(\boldsymbol{a})\boldsymbol{\Theta}(\boldsymbol{a}) \tag{38a}$$

$$\bar{\boldsymbol{C}}(\boldsymbol{a}) \triangleq \boldsymbol{\Theta}(\boldsymbol{a})^T \boldsymbol{C}(\boldsymbol{a})\boldsymbol{\Theta}(\boldsymbol{a}) \tag{38b}$$

$$\bar{\boldsymbol{K}}(\boldsymbol{a}) \triangleq \boldsymbol{\Theta}(\boldsymbol{a})^T \boldsymbol{K}(\boldsymbol{a})\boldsymbol{\Theta}(\boldsymbol{a}) \tag{38c}$$

$$\bar{\boldsymbol{u}}(t) \triangleq \boldsymbol{\Theta}(\boldsymbol{a})^T \boldsymbol{u}(t) \tag{38d}$$

$\bar{\boldsymbol{M}}(\boldsymbol{a})$, $\bar{\boldsymbol{C}}(\boldsymbol{a})$, and $\bar{\boldsymbol{K}}(\boldsymbol{a})$ are the generalized mass, damping, and stiffness matrices for a given damaged case, respectively, and $\bar{\boldsymbol{u}}(t)$ is the generalized control vector. These generalized matrices are used to calculate the discrete-time state transition matrix $\boldsymbol{\Phi}_{k+1,k}$ using Eqs. (19) and (6) and the control matrix $\boldsymbol{\Psi}_{k+1,k}$ using Eq. (7). The original, discrete-time state vector $\boldsymbol{x}_k$, which includes the finite element degrees of freedom, is transformed to a new state

**Table 1 Blade properties**

| Parameter | Value |
|---|---|
| Radius $R$ | 6.7 m |
| Chord $c$ | 0.39 m |
| Thickness $h$ | 3.9 cm |
| Baseline stiffness $EI_0$ | $2.3 \times 10^4$ N · m$^2$ |
| Mass per unit length $\lambda$ | 6.05 kg/m |
| Damping coefficient $\zeta$ | 0.01 |
| Number of elements $N$ | 20 |

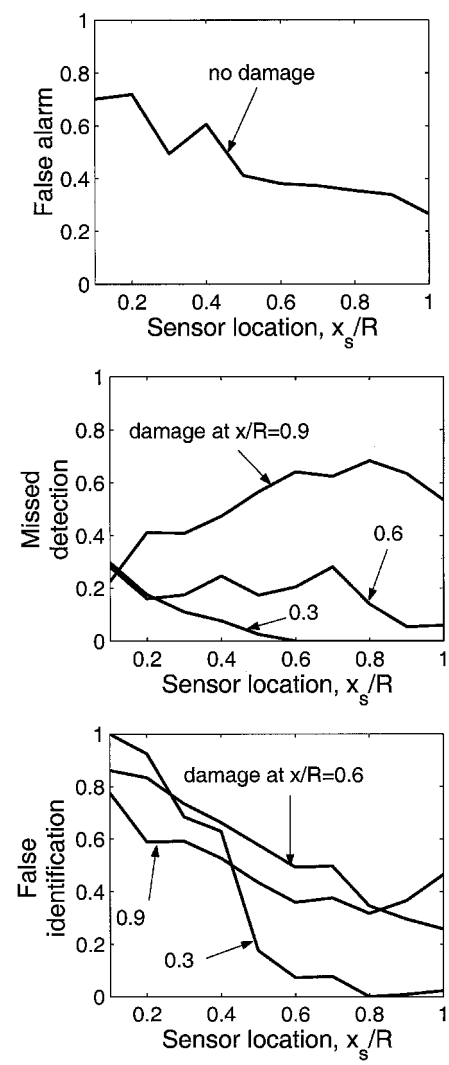


**Fig. 4 Performance measures.**

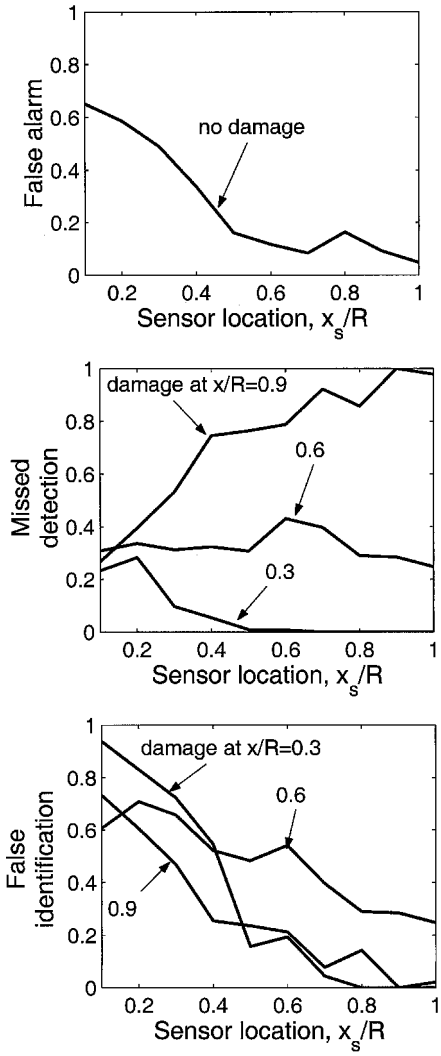


**Fig. 5 Performance measures; model of damage at tip eliminated.**

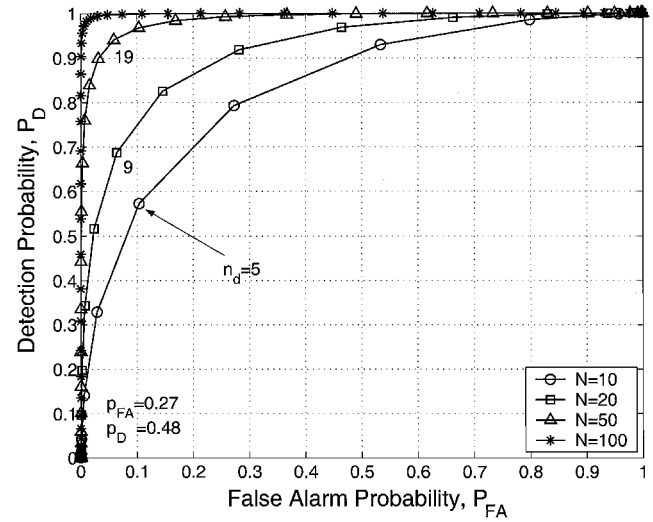


**Fig. 6 Detector operating characteristics for the case of a tip damage and tip sensor.**

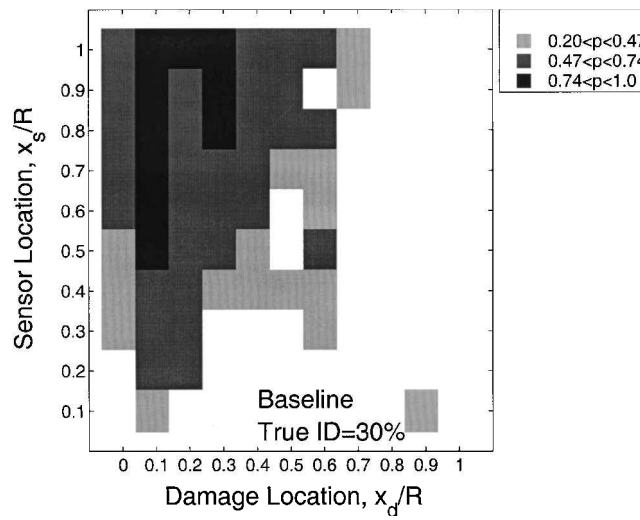


**Fig. 7 Damage identification results for baseline case.**

vector $\xi_k$, which comprises the modal participation factors. Substituting Eq. (35) into Eq. (2) ensures that the measurements are kept displacement/rotations in nature, although the state vector is transformed. The first five modal shapes of both the baseline and the damaged cases are calculated and used in each filter's discrete propagation and updating equations. The main advantage of this modal representation arises from the significantly reduced model size, allowing smaller (and, therefore, faster) filters to be implemented.

The noisy measurement information is based on one sensor located at one of 10 equally spaced possible nodes along the blade. The sampling frequency is 20 Hz. In each of the possible cases a $t_p = 4$ s detection time interval is given to the multiple-model identification algorithm, of which the last $t_d = 1$ s comprises the decision time interval. The single-run detection and identification capabilities are demonstrated in Figs. 4–8. In these cases, the first mode of the blade is excited by an initial tip deflection (initial velocity is zero), where the only external load comes from the blade's own weight. The measurement taken is a single vertical displacement at one of the FE nodes. The measurement noise standard deviation equals 0.5 mm.

In Fig. 4, three single-run performance measures of the proposed detection and identification algorithm are examined: false alarm, missed detection, and false identification rates, all presented vs sensor location along the blade. False alarm rate is defined as the probability of detecting damage when no damage occurs. Missed detection is the probability of obtaining the output "no damage" when damage indeed occurs along the blade. The probability of false identification is defined, in this study, as the probability of correctly detecting the presence of damage, albeit in a wrong location. As seen from Fig. 4, the false alarm rate is fairly high even in cases where the sensor is located near the tip. This phenomenon can be explained by considering that two of the filters, in this particular damage detection problem, have small, even insignificant, differences between them, namely, the filter representing damage close to the blade's tip and the undamaged one. Because damage close to the tip causes no significant changes in displacement, the differences in the residuals of these two filters fade away when noise is present. Thus, in some cases, the true undamaged case is identified incorrectly as damage near the tip. To demonstrate the preceding assumption, the filter representing damage near the tip was removed from the bank of filters. Now, as seen from Fig. 5, the false alarm rate decreases significantly. However, the missed detection rate of damage near the tip increases because no model represents this case adequately. Concluding this discussion, it is evident that the case of damage near the tip is less observable and should be treated separately using additional models.

A statistical experiment composed of several repetitions of a single-run process enables some control on the overall false alarm and detection probabilities. The results of such an experiment depend on $p_{\mathrm{FA}}$ and $p_D$, as discussed in Sec. V. As an example, consider the problematic case of a damage close to the tip ($x/R = 0.9$) along with a sensor located at the tip ($x_s/R = 1$). As seen from Fig. 4, the single-run false alarm rate and detection probability correspond to unacceptable values of 0.27 and 0.48, respectively. Figure 6 is a detector operating characteristics representation, showing the number of repetitions $N$ needed along with the appropriate threshold level $n_d$ to achieve reasonable overall false alarm and detection probabilities.

For example, choosing $N = 50$ and $n_d = 19$ gives an overall false alarm rate of 0.06 and a detection probability of 0.95.

The shaded areas in Figs. 7 and 8 comprise all of the cases in which the true damage was identified. (This is the case where the model associated with $q_{\max}$ represents damage location closest to the true damage location.) The first column (zero damage location) represents the no-damage case. Let $p$ denote the probability of correct identification for a specific damage and sensor locations, defined as $p \triangleq N_c / N_{\mathrm{MC}}$, where $N_c$ corresponds to the number of Monte Carlo runs in which correct identification was achieved and $N_{\mathrm{MC}}$ is the total number of Monte Carlo runs. Three levels of confidence are shown, each one corresponding to an interval of values of $p$. Let $\bar{q}_{\max}(x_d, x_s)$ be defined as

$$\bar{q}_{\max}(x_d, x_s) \triangleq \begin{cases} q_{\max} & \text{correct identification achieved} \\ 0 & \text{no identification} \end{cases} \tag{39}$$

Then, the percentage given in Fig. 7, and also later on, is given by

$$\text{true identification} = \frac{\sum_{x_d=0}^{1} \sum_{x_s=0.1}^{1} \bar{q}_{\max}(x_d, x_s)}{110} \tag{40}$$

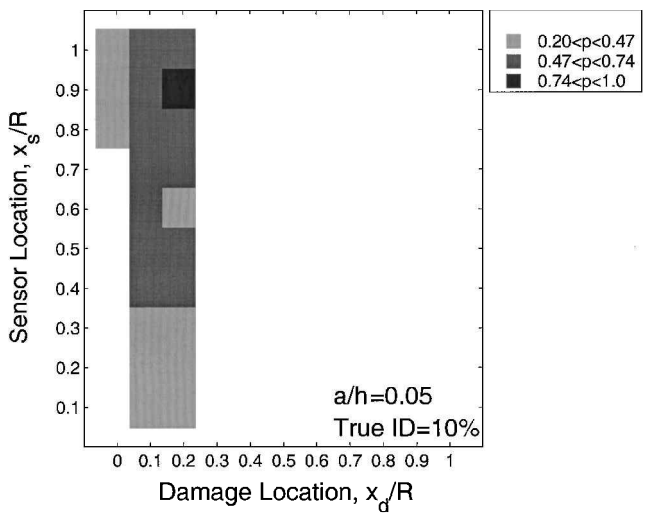


***a/h* = 0.05**

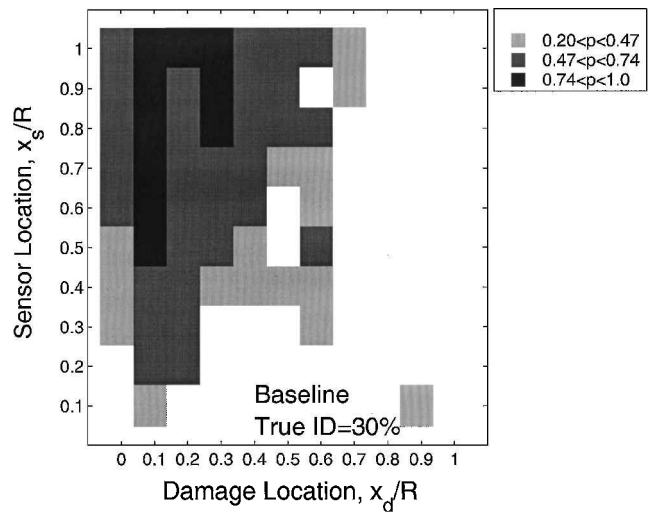


***a/h* = 0.2**

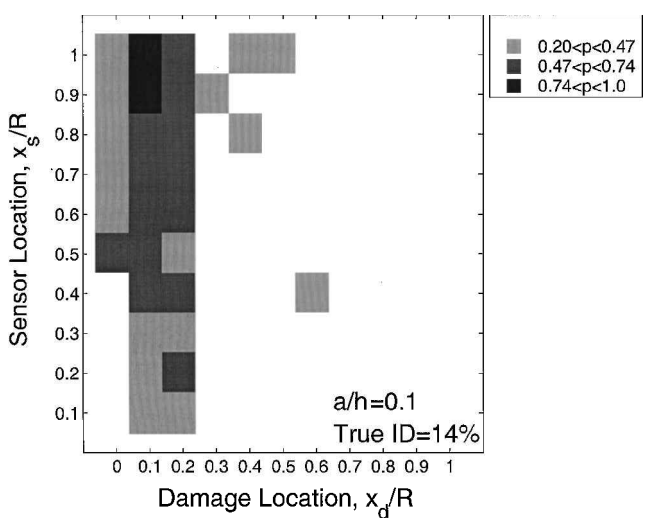


***a/h* = 0.1**

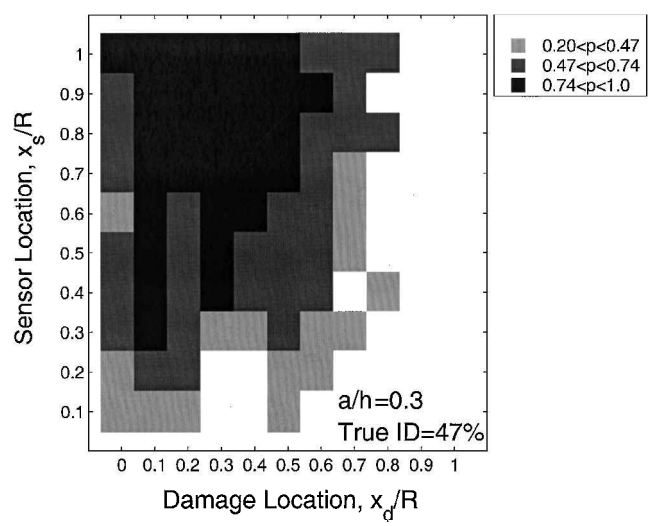


***a/h* = 0.3**

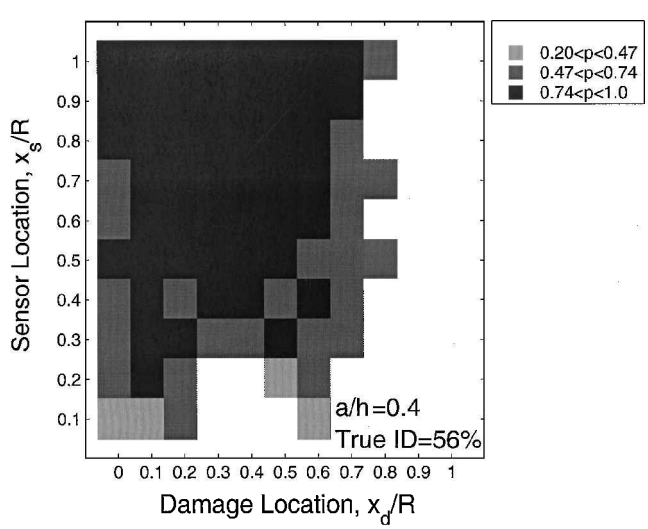


***a/h* = 0.4**

**Fig. 8 Damage identification results for several damage intensities.**

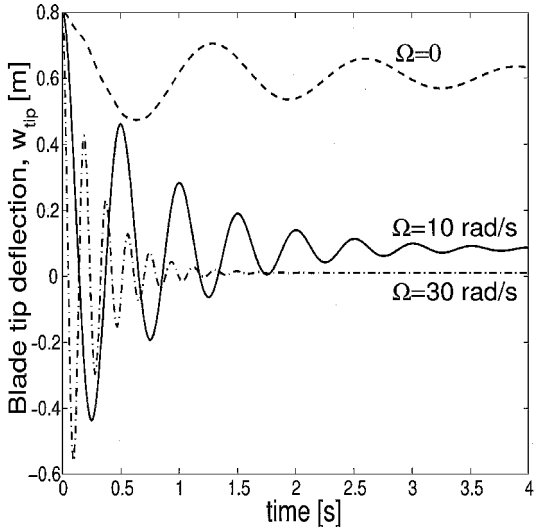


**Fig. 9 Rotating blade tip response to first mode excitation ($\zeta = 0.1$).**

where $x_d$ is the damage location and $x_s$ refers to the sensor location. As shown in Fig. 7, damage located close to the fixed end of the blade is more observable. Moreover, a sensor located close to the tip also enhances detection capability. This results from the fact that damage near the fixed end has the most significant influence on the vertical displacements along the beam. In addition, the noise level is kept constant; therefore, the signal-to-noise ratio decreases toward the fixed end, preventing correct identification. The identification of "inboard damage" (i.e., damage located inboard relative to the sensor) is of higher quality and reliability. On the other hand, detection of "outboard damage" (i.e., damage located outboard relative to the sensor) is more complicated due to the relatively little information contributed inboard by a crack compared with the information contributed outboard. In some cases, however, outboard damage is detected due to small differences in modal shapes between the damaged models and the undamaged baseline case. Also, during the short blade's transient response time, dynamic effects may become significant, so that outboard damage detectability is achieved.

A parametric study was carried out, investigating the effects of various parameters under consideration.[13] Figure 8 demonstrates the effect of increased damage level. As can be expected from before, the detection capability increases as the damage level increases. Typically, sensors located near the tip give the best results. Small cracks can be detected using this algorithm only when located near the fixed end of the blade. Large cracks are easily detected even when the sensor is located inboard relative to the crack location.

The case of a rotating blade excited by an initial tip deflection (equal to the excitation in the baseline case) was also examined.[13] Here, the tip displacement initial condition is identical for all examined cases. However, the steady-state displacement depends on the specific angular velocity. Hence, the initial to steady-state displacement ratio increases with increased angular velocity, as shown in Fig. 9. (The blade's structural damping $\zeta$ is increased to 0.1 to demonstrate the aforementioned effect.) This enhances the damage detection capability. On the other hand, the blade's angular velocity contributes to the total stiffness (as shown in Fig. 10), hence, causing a decrease in the settling time, allowing the filters less time to perform the identification process. The results in Ref. 13 show that damage detection capability decreases as the blade's angular velocity increases.

### B. Full-Scale, Fixed-Shaft Rotor

Consider a full-scale cantilevered two-bladed fixed-shaft rotor in vacuum with blade properties listed in Table 2. A deformed cantilevered blade is schematically presented in Fig. 11. In this case, three elastic modes are considered: the first beamwise (flap) bending mode, the first chordwise (lead-lag) bending mode, and the first twist mode. Here, the damage is manifested as a 10% reduction in both the beamwise and the chordwise stiffnesses, as well as in the torsional rigidity, at a specific blade element. The rotor analysis has

**Table 2 Rotor properties**

| Parameter | Value |
|---|---|
| Radius $R$ | 8.2 m |
| Chord $c$ | 0.53 m |
| Beamwise stiffness $EI_b$ | $7.62 \times 10^4$ N · m$^2$ |
| Chordwise stiffness $EI_c$ | $1.72 \times 10^5$ N · m$^2$ |
| Torsional rigidity $GJ$ | $8.57 \times 10^4$ N · m$^2$ |
| Tensile stiffness $AE$ | $2.97 \times 10^9$ N |
| Mass per unit length $\lambda$ | 10 kg/m |
| Angular velocity $\Omega$ | 27 rad/s |

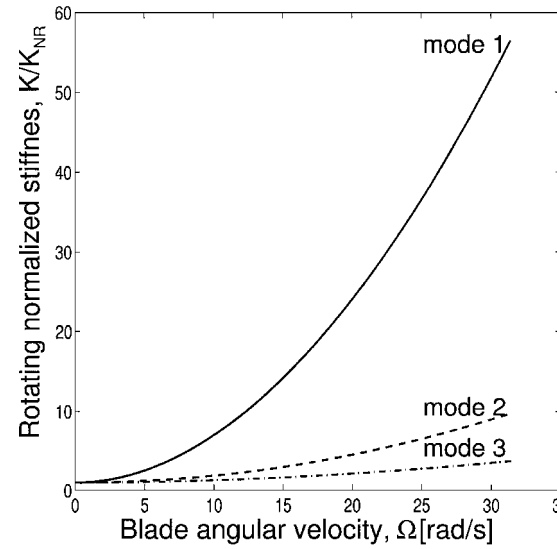


**Fig. 10 Normalized modal stiffness vs blade angular velocity.**

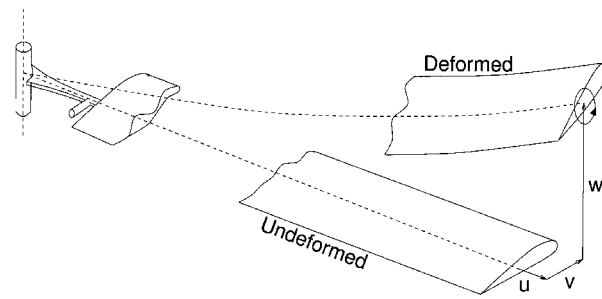


**Fig. 11 Deformed elastic blade.**

been carried out using the software package RAPID/Plus,[14] which is capable of modeling general rotorcraft configurations, conventional helicopters, and tilt rotors. RAPID/Plus may handle nonuniform and dissimilar blades and is, therefore, suitable to the current task. Both rigid and elastic blade analyses are possible. Blade elasticity is modeled using a built-in modal-based analysis for structurally pretwisted spars. This analysis enables including the blade's axial, lead-lag, flap, and twist elastic deformations, designated by $u$, $v$, $w$, and $\phi$, respectively. The software package also enables the inclusion of fully articulated blades (not used in this study) with arbitrary pitch, flap, and lag offsets; root springs and dampers; and a detailed control system mechanism (swashplate, elastic pitch links, pitch horn, etc.), which enables future study of faults in these components. Although it is assumed, in this study, that the undamaged blades are identical, it is by no means a necessary condition. The ability to handle dissimilar blades may also be used to model an undamaged case with nonidentical blades.

The equations of blade motions are derived using RAPID/Plus.[14] The system matrices are then utilized for constructing the bank of Kalman filters. In this case, the damaged models are spread along the blade as stated earlier in Sec. VI.A; however, the damage is assumed to occur only in one of the blades, designated as blade 1. Moreover, the models account for damage only in blade 1.

Three measurements are taken at a specific node along blade 1, two velocity components (vertical and horizontal), and one angular

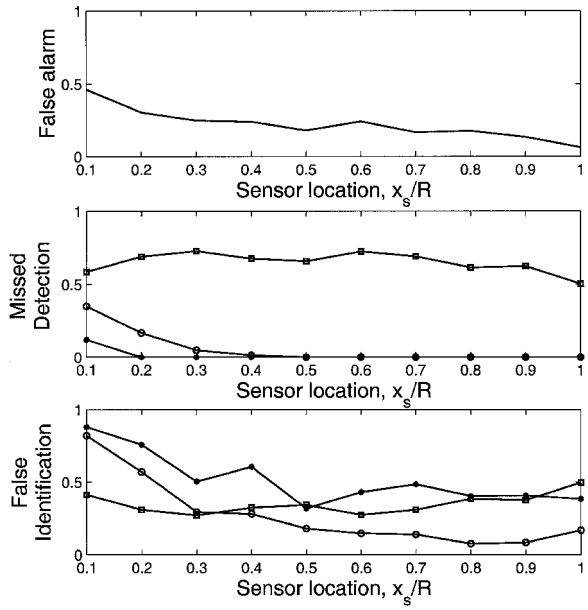


**Fig. 12 Performance measures, case of a full-scale damaged rotor: ——, no damage; ●, damage at $x/R = 0.3$; ○, damage at $x/R = 0.6$; and □, damage at $x/R = 0.9$.**

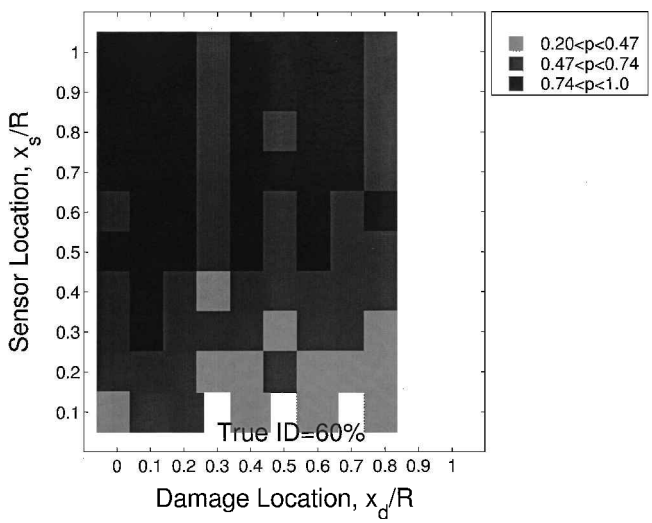


**Fig. 13 Rotor damage identification results.**

velocity (pitch rate). The measurement noise standard deviation is ±0.1 m/s for velocity and ±0.1 rad/s for angular velocity. (These values correspond to a signal-to-noise ratio of 10 for measurements taken at the blade's tip.) For this case, four rotor revolutions are taken as the detection time interval, whereas the decision time is the last revolution. Figure 12 shows the single-run three performance measures defined earlier, whereas Fig. 13 shows the single-run damage identification results. As demonstrated in Figs. 12 and 13, damage detectability using the proposed method is fairly high at most sensor locations. The high false alarm rate, for sensors located near the blade's root, originates from the relatively low signal-to-noise ratio (10 at tip, less than 10 inboard) adopted in the present results. Here also, as demonstrated in Sec. VI.A, the use of a statistical experiment enables improving the overall false alarm and detection probabilities by choosing an appropriate number of repetitions $N$ and threshold level $n_d$.

In passing, some remarks are in order concerning the use and implementability of the proposed new FDI method.

*Remark 2*: In practice, it can be expected that some variations will exist between (undamaged) production blades. This gives rise to the question of how well the proposed method can cope with structural modeling uncertainties. Recent results, presented in Ref. 13, show that the proposed FDI algorithm provides good performance, even when some variations are applied to some of the system parameters. (Up to 20% variation was implemented in the study presented in Ref. 13.) These variations may also represent the case of undamaged, but slightly different, blades.

*Remark 3*: The computer simulations performed during the course of this study have proved that the new method can be implemented in real-time using current computer technology.

*Remark 4*: The noise levels used in the computer simulations were very conservative. In practice, lower noise levels are expected, allowing prediction of even better detection and identification performance.

## VII. Conclusions

A model-based damage detection algorithm for rotating blades, using an adaptive estimation technique, incorporating noisy measurements, is presented. When rotary mechanical systems are considered, the algorithm presented constitutes a new application of the adaptive estimation approach, to the best of the authors' knowledge. The damage detection capability is tested in various cases. In general, for low noise levels, this approach provides excellent damage identification results. For the case of a flapping only blade, it is shown that, typically, a sensor located near the blade's tip gives the best results. In some cases, when several modes are excited, a sensor located inboard relative to the crack location contributes valuable information, thus enhancing the detection capability. The results for the case of a full-scale rotor clearly indicate good damage detectability, even in the presence of a relatively high level of noise. The proposed method enables various types of rotor faults and sensors to be implemented.

Only cantilevered blade results are presented in this paper. However, the methodology presented herein is not limited to this particular type of blade. In fact, the same methodology is expected to be adequate for the analysis of other types of rotor blades as well.

## References

[1] Kahl, K., and Sirkis, J. S., "Damage Detection in Beam Structures Using Subspace Rotation Algorithm with Strain Data," *AIAA Journal*, Vol. 34, No. 12, 1996, pp. 2609–2614.

[2] Ostachowicz, W. M., and Krawczuk, M., "Analysis of the Effect of Cracks on the Natural Frequencies of a Cantilever Beam," *Journal of Sound and Vibration*, Vol. 150, No. 2, 1991, pp. 191–201.

[3] Sundermeyer, J. N., and Weaver, R. L., "On Crack Identification and Characterization in a Beam by Non–Linear Vibration Analysis," *Journal of Sound and Vibration*, Vol. 183, No. 5, 1995, pp. 857–871.

[4] Yuen, M. M. F., "A Numerical Study of the Eigenparameters of a Damaged Cantilever," *Journal of Sound and Vibration*, Vol. 103, No. 3, 1985, pp. 301–310.

[5] Kiddy, J., and Pines, D. J., "Eigenstructure Assignment Technique for Damage Detection in Rotating Structure," *AIAA Journal*, Vol. 36, No. 9, 1998, pp. 1680–1685.

[6] Kiddy, J., and Pines, D. J., "Experimental Validation of a Damage Detection Technique for Helicopter Main Rotor Blades," *Journal of Systems and Control Engineering*, Vol. 215, No. 3, Pt. 1, 2001, pp. 209–220.

[7] Kiddy, J., and Pines, D., "The Effects of Aerodynamic Damping on Damage Detection in Helicopter Main Rotor Blades," *55th Annual Forum Proceedings*, American Helicopter Society, Alexandria, VA, 1999, pp. 2387–2395.

[8] Magill, D. T., "Optimal Adaptive Estimation of Sampled Stochastic Processes," *IEEE Transactions on Automatic Control*, Vol. AC–10, No. 4, 1965, pp. 434–439.

[9] Maybeck, P. S., *Stochastic Models, Estimation, and Control*, Vol. 2, Academic Press, New York, 1982, pp. 129–136.

[10] Mendel, J. M., *Lessons in Digital Estimation Theory*, Prentice–Hall, Upper Saddle River, NJ, 1987, pp. 149–159.

[11] Stepaniac, M. J., and Maybeck, P. S., "MMAE–based Control Redistribution Applied to the VISTA F–16," *IEEE Transactions on Aerospace and Electronic Systems*, Vol. 34, No. 4, 1998, pp. 1249–1259.

[12] Bielawa, R. L., *Rotary Wing Structural Dynamics and Aeroelasticity*, AIAA Education Series, AIAA, Washington, DC, 1992, pp. 63–109.

[13] Alkahe, J., "Helicopter Faults, Simulation, Detection and Identification," Ph.D. Dissertation, Dept. of Aerospace Engineering, Technion—Israel Inst. of Technology, Haifa, Israel, March 2002.

[14] Rand, O., "RAPID/Plus: Rotorcraft Analysis for Preliminary Design + Aeroelasticity: User Manual," Dept. of Aerospace Engineering, Technion—Israel Inst. of Technology, TR TAE-831, Haifa, Israel, Jan. 1999.